Title

Mechanistic Investigation, Wavelength-Dependent Reactivity, and Expanded Reactivity of N—Aryl Azacycle Photomediated Ring Contractions

Journal

Journal of the American Chemical Society, 146(8)

ISSN

0002-7863

Authors

Kim, Sojung F
Schwarz, Henrik
Jurczyk, Justin
et al.

Publication Date

2024-02-28

DOI

10.1021/jacs.3c13982

Peer reviewed

Published in final edited form as:

J Am Chem Soc. 2024 February 28; 146(8): 5580–5596. doi:10.1021/jacs.3c13982.

Mechanistic Investigation, Wavelength-Dependent Reactivity, and Expanded Reactivity of *N*–Aryl Azacycle Photomediated Ring Contractions

Sojung F. Kim,
Department of Chemistry, University of California, Berkeley, Berkeley, California 94720, United States

Henrik Schwarz,
Department of Chemistry, University of California, Berkeley, Berkeley, California 94720, United States; Present Address: Institute of Organic Chemistry, Leibniz Universität Hannover, 30167 Hannover, Germany

Justin Jurczyk,
Department of Chemistry, University of California, Berkeley, Berkeley, California 94720, United States; Present Address: Gilead Sciences, Inc., 333 Lakeside Drive, Foster City, California 94404, United States.

Bailey R. Nebgen,
Department of Chemistry, University of California, Berkeley, Berkeley, California 94720, United States; Lawrence Berkeley National Laboratory, Materials Sciences Division, Berkeley, California 94720, United States

Hailey Hendricks,
Department of Discovery Chemistry, Merck & Co., Inc., Boston, Massachusetts 02115, United States; Present Address: Department of Chemistry, Princeton University, Princeton, New Jersey 08544, United States.

Corresponding Authors Michael W. Zuerch – Department of Chemistry, University of California, Berkeley, Berkeley, California 94720, United States; Lawrence Berkeley National Laboratory, Materials Sciences Division, Berkeley, California 94720, United States; mwz@berkeley.edu; **Kaid Harper** – Process Chemistry, Abbvie Inc., North Chicago, Illinois 60064, United States; kaid.harper@abbvie.com; **Michaelyn C. Lux** – Department of Discovery Chemistry, Merck & Co., Inc., Boston, Massachusetts 02115, United States; michaelyn.lux@merck.com; **Charles S. Yeung** – Department of Discovery Chemistry, Merck & Co., Inc., Boston, Massachusetts 02115, United States; charles.yeung@merck.com; **Richmond Sarpong** – Department of Chemistry, University of California, Berkeley, Berkeley, California 94720, United States; rsarpong@berkeley.edu.

Author Contributions

All authors have given approval to the final version of the manuscript.

Supporting Information

The Supporting Information is available free of charge at https://pubs.acs.org/doi/10.1021/jacs.3c13982.

Experimental procedures, optimization, characterization data, NMR spectra for all compounds, UV–Vis data, kinetic experiments, quantum yield determination, model of inner filter effect on rate, crystallographic data, computational details, and Cartesian coordinates of DFT-optimized structures (PDF)

Accession Codes

CCDC 2309251–2309255 contain the supplementary crystallographic data for this paper. These data can be obtained free of charge via www.ccdc.cam.ac.uk/data_request/cif, by emailing data_request@ccdc.cam.ac.uk, or by contacting The Cambridge Crystallographic Data Center, 12 Union Road, Cambridge CB2 1EZ, U.K.; fax: + 44 1223 336033.

The authors declare the following competing financial interest(s): R.S. is a paid consultant for MSD. The authors declare no other competing interests.

Hojoon Park,
Department of Process Research and Development, Merck & Co., Inc., Boston, Massachusetts 02115, United States

Andrew Radosevich,
Small Molecule Therapeutics & Platform Technologies, Abbvie Inc., North Chicago, Illinois 60064, United States

Michael W. Zuerch,
Department of Chemistry, University of California, Berkeley, Berkeley, California 94720, United States; Lawrence Berkeley National Laboratory, Materials Sciences Division, Berkeley, California 94720, United States

Kaid Harper,
Process Chemistry, Abbvie Inc., North Chicago, Illinois 60064, United States

Michaelyn C. Lux,
Department of Discovery Chemistry, Merck & Co., Inc., Boston, Massachusetts 02115, United States

Charles S. Yeung,
Department of Discovery Chemistry, Merck & Co., Inc., Boston, Massachusetts 02115, United States

Richmond Sarpong
Department of Chemistry, University of California, Berkeley, Berkeley, California 94720, United States

Abstract

Under mild blue-light irradiation, α-acylated saturated heterocycles undergo a photomediated one-atom ring contraction that extrudes a heteroatom from the cyclic core. However, for nitrogenous heterocycles, this powerful skeletal edit has been limited to substrates bearing electron-withdrawing substituents on nitrogen. Moreover, the mechanism and wavelength-dependent efficiency of this transformation have remained unclear. In this work, we increased the electron richness of nitrogen in saturated azacycles to improve light absorption and strengthen critical intramolecular hydrogen bonding while enabling the direct installation of the photoreactive handle. As a result, a broadly expanded substrate scope, including underexplored electron-rich substrates and previously unsuccessful heterocycles, has now been achieved. The significantly improved yields and diastereoselectivities have facilitated reaction rate, kinetic isotope effect (KIE), and quenching studies, in addition to the determination of quantum yields. Guided by these studies, we propose a revised ET/PT mechanism for the ring contraction, which is additionally corroborated by computational characterization of the lowest-energy excited states of α-acylated substrates through time-dependent DFT. The efficiency of the ring contraction at wavelengths longer than those strongly absorbed by the substrates was investigated through wavelength-dependent rate measurements, which revealed a red shift of the photochemical action plot relative to substrate absorbance. The elucidated mechanistic and photophysical details effectively rationalize empirical observations, including additive effects, that were previously poorly understood. Our findings not only demonstrate enhanced synthetic utility of the photomediated

ring contraction and shed light on mechanistic details but may also offer valuable guidance for understanding wavelength-dependent reactivity for related photochemical systems.

Graphical Abstract

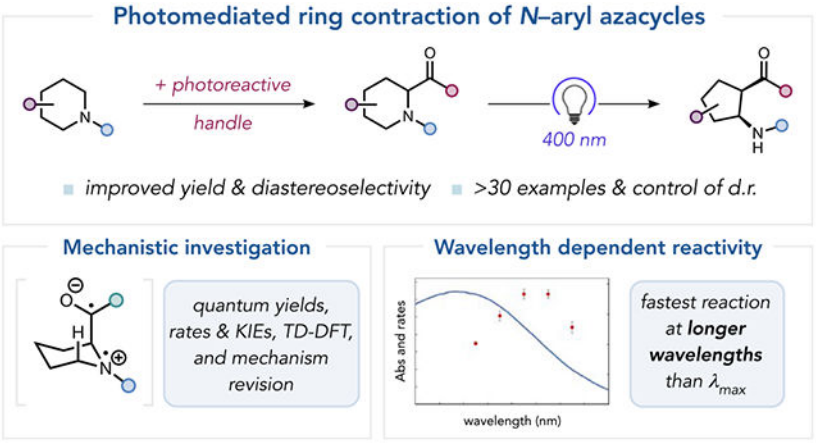

INTRODUCTION

Methods for single-atom skeletal editing, which precisely delete, add, or swap atoms without the need for *de novo* synthesis (Figure 1A), can expedite the discovery of novel bioactive molecules,[1] rapidly expand accessible chemical space, and revolutionize retrosynthesis and molecular design.[2-4] Saturated heterocycles, particularly those containing nitrogen, are ideal targets for skeletal editing methods due to their ubiquity in pharmaceutical and agrochemical molecules, in addition to their high sp^3 content.[5-8] In fact, 88% of the FDA-approved small-molecule drugs reported from 2015 to 2020 contain at least one *N*-heterocycle.[9] These reactions would efficiently modify the cores of such privileged motifs, enabling rapid scaffold hopping to expedite the exploration of bioactivity.[10,11] However, developing mild and general skeletal editing transformations of saturated heterocycles is particularly challenging due to the relative inertness of their ubiquitous $C(sp^3)$—$C(sp^3)$ bonds.[3,12]

To this end, our group and others have sought to develop single-atom skeletal editing techniques focused on modifying heterocycles by deleting or inserting nitrogen, carbon, oxygen, or sulfur atoms.[2,3,13-18] In 2021, we reported the photomediated ring contraction of saturated heterocycles (Figure 1B).[13] Using 400 nm blue-light irradiation, α-acylated saturated heterocycles underwent a one-atom ring contraction to afford functionalized five-membered ring products, wherein the α-acyl heteroatom had undergone an endo-to-exocyclic migration.[13] This methodology exemplified a single-atom extrusion under mild conditions, which rapidly afforded novel vectors for additional bond formations and biological interactions. Specifically for derivatives of piperidine, the third most frequently encountered ring system in small-molecule FDA-approved drugs as of 2020,[7] the ring contraction yielded derivatized aminocyclopentanes that themselves are valuable biorelevant targets.[7,19,20]

As part of our initial exploration of the photomediated ring contraction, we demonstrated the transformation on 49 substrates (Figure 1B depicts an abbreviated scope), including drug derivatives, cyclic peptides (**13** to **14**), and sugars[13]. While *N*-arylsulfonyl piperidines contracted in the highest yields (e.g., **1**), substrates bearing other electron-withdrawing substituents on nitrogen, such as phosphoramidite (**2**) and acyl (**3**, **4**) groups, successfully contracted in the presence of 3-cyanoumbelliferone as an additive. This additive was identified in a high-throughput screen of photocatalysts and photosensitizers and modestly increased the yield (approximately 11%) and diastereoselectivity for some substrates. However, the origin of this effect was poorly understood, as efficient triplet sensitization was precluded by the lower triplet energy of 3-cyanoumbelliferone relative to the substrates.

Other heterocycles, including tetrahydropyrans (**9**) and cyclic thianes (**11**), also efficiently contracted to yield cyclopentane alcohols and thiols (**10** and **12**), respectively. Computational analysis revealed that hydrogen bonding and steric repulsions in the Mannich ring-closing transition state favored *cis*-diastereoselectivity in the product-forming transition state (Figure 1B, bottom). Additionally, the intermediate imine-enol was determined to predominantly form and react from the (*E/Z*) and (*E/E*) geometries.

Although the photoreactive aroyl (aryl ketone) motif is preserved in the ring contraction products (e.g., see **11** to **12**), the selective reactivity of the starting material in the presence of the product under continued irradiation was observed. This selectivity was rationalized by an experimentally measured and calculated hypsochromic shift and decrease in intensity of the $n \rightarrow \pi^*$ absorption for the products due to intramolecular H-bonding between the extruded amine and carbonyl.[13] However, given that the substrates absorb weakly at 400 nm ($\lambda_{max,\ n \rightarrow \pi^*} = 340$ nm), the empirically established optimal LED irradiation centered at 400 nm could not be fully reconciled with the observed reactivity. Finally, we reported initial efforts toward a general asymmetric variant; the addition of substoichiometric amounts of chiral phosphoric acid rendered the contraction enantioselective by accelerating the Mannich ring closure.

Despite our extensive investigation into the photomediated ring contraction, the scope of azacycles was limited to substrates bearing electron-withdrawing groups on nitrogen. Indeed, one of the most significant current challenges in the field of single-atom heterocycle skeletal editing is method generalization, ensuring that the scope is broad enough so that these techniques are versatile and synthetically useful on diverse compounds.[2] Though new skeletal editing methods have great potential, their real-world application to the discovery or synthesis of a broad range of molecules necessitates robust and context-independent reactivity. In our initial investigation, the substrate limitation was, in part, an artifact of substrate synthesis that typically began from commercially available piperidines that already bore the photoreactive aroyl handle. However, having to build more complex substrates around such a prefunctionalized scaffold limits the broader utility of this chemistry, especially for the late-stage diversification of bioactive molecules which do not frequently contain phenone groups. Moreover, the relatively modest product yields and diastereoselectivity outcomes, in addition to the poorly understood wavelength-dependent efficiency and role of the 3-cyanoumbelliferone additive, made further mechanistic investigation beyond computational efforts challenging.

To address these challenges, we identified *N*-aryl substrates as attractive, underexplored, and electronically differentiated targets for method generalization for several reasons (Figure 1C). We hypothesized that increasing the electron density on nitrogen by swapping the previously explored electron-withdrawing substituents (sulfonyl, acyl groups, etc.) for aromatic rings would improve the diastereoselectivity and photostability of the products by strengthening intramolecular H-bonding interactions to the more basic nitrogen lone pair. The higher energy lone pair on nitrogen could also alter the absorption characteristics of the substrates or related photophysical processes. The electron richness of these substrates would also enable us to leverage emerging chemistries to install the photoreactive aroyl handle on a wide range of compounds, broadening synthetic utility.[21-23] Within the framework of skeletal editing, the ability to install the requisite photoreactive handle on any desired *N*–Ar heterocycle would prevent the need for a lengthy, inefficient synthesis of targeted substrates from prefunctionalized precursors. From a practical standpoint, these precursor *N*–aryl compounds are readily accessible through precedented C—N cross-coupling methods (Buchwald–Hartwig, Ullman, etc.) and are prevalent in bioactive molecules.[24]

In this paper, we report the photomediated ring contraction of *N*-arylated saturated azacycles. Compared to our prior work,[13] significantly improved yields and diastereoselectivities were observed, in part resulting from improved light absorption of the substrates and stronger intramolecular H-bonding. Subtle effects of additives on the system that were previously poorly understood are elucidated. To improve synthetic utility, conditions that enable the control of diastereoselectivity are disclosed. Improved reactivity has both enabled the successful ring contraction of previously challenging substrate classes and facilitated the investigation of the mechanism and excitation behavior of the substrates. Kinetics experiments support a mechanism involving photon-limited reactivity, where productive excitation is rate-determining. On the basis of experimental KIE and triplet quenching studies, we propose a mechanism wherein the excited-state substrates undergo rapid intramolecular SET to the carbonyl from the nitrogen lone pair followed by deprotonation to afford a 1,4-biradical intermediate, which undergoes a ring-opening and -closing sequence to afford the aminocyclopentane products. This mechanism, which is a revision of our previous proposal,[13] is further corroborated by computational characterization of the lowest-energy excited states of *α*-acylated substrates through time-dependent DFT (TDDFT), as well as observed trends in measured quantum yields and molar extinction coefficients. Finally, our investigation of wavelength-dependent rates reveals a significant red shift between the photochemical action plot and UV–Vis absorbance of the substrates, indicating that wavelengths between 395 and 405 nm are most efficient at promoting the desired ring contraction despite the substrates weakly absorbing at those wavelengths. Potential explanations for why the substrate UV–Vis absorbance spectrum fails to accurately predict optimum reactivity are discussed.

RESULTS AND DISCUSSION

Installation of the Photoreactive Handle.

The ability to install the photoreactive ketone (often aroyl) α- to the nitrogen of *N*-functionalized piperidine derivatives would expand the synthetic utility and broaden the scope of the photomediated ring contraction by accommodating a wider variety of heterocyclic compounds. Rather than requiring lengthy syntheses to incorporate a pre-aroylated piperidine early on in a synthetic sequence, this strategy would render any substrate of interest photoreactive by directly installing the aroyl group. One could then perform the ring contraction and potentially remove or further functionalize the aroyl group if desired. Ultimately, this strategy would require peripheral functionalization of saturated heterocycles (installation of the aroyl group) in order to effect a skeletal edit (i.e., ring contraction), which could then be followed by further peripheral modifications as desired (Figure 2A).[14] Ideally, the overall transformation would constitute a short synthetic sequence that enables efficient access to derivatives with high structural diversity.

The relative electron richness of the *N*–Ar substrates opens up several avenues for oxidation that would enable α-functionalization through precedented α-amino radical or iminium intermediates (Figure 2B).[21,25] Initial efforts focused on leveraging emerging photomediated α-acylation techniques, including those reported by Montgomery, Doyle, and Xu.[22,25-29] The Xu aroylation chemistry was most applicable for our desired *N*–aryl substrate classes (Figure 2C), as we had previously identified aryl ketones as the most effective photoreactive handle (as opposed to aliphatic acyl groups or other functional groups). While photomediated aroylation worked well for most *N*–aryl precursors, substrates bearing more electron-deficient groups, such as *N*–pyridyl moieties, were not successfully aroylated. This limitation is likely due to the inability of the photocatalyst to oxidize the parent *N*–aryl amines in these cases, which is required to generate α-amino radicals for downstream radical–radical coupling.[27] However, screening more oxidizing photocatalysts did not significantly improve the yields. Alternative routes to directly access the desired substrates were investigated and found to be unsuccessful or similarly limited in terms of scope (for details, see the SI).[29-38]

To supplement the scope of the α-aroylation, some substrates were accessed through multistep syntheses. However, in most cases, the direct installation of the photoreactive handle onto *N*-aryl amine building blocks proved to be the most efficient route to the desired substrates.

Photomediated Ring Contraction.

Irradiation of the α-aroylated azacyclic substrates was carried out using a Penn PR m2 photoreactor equipped with a 400 nm LED insert.[39] Solvent screening with model *N*–Ph substrate **15** led to the identification of THF as the optimal solvent that maximizes the yield and diastereoselectivity of the photomediated ring contraction of this new substrate class (see SI section 3 for details). Of note, THF is also significantly less toxic and more environmentally friendly than benzene, which had previously been identified as the optimal solvent for substrates bearing electron-withdrawing groups on nitrogen.[13,40] High yields

and greater than 20:1 *cis*-diastereoselectivity were observed for the products in nearly all organic solvents screened, with ethereal solvents generally affording the highest yields. The observed *cis*-diastereoselectivity is consistent with our previous observations,[13] and arises from a combination of H-bonding and steric repulsions in the Mannich ring-closing transition state that favors *cis* products (see, for example, Figure 1B, bottom).

The ring contraction is relatively robust; trace water from solvents or glassware that were not rigorously dried had no significant effect on yield or diastereoselectivity, and running the reaction completely open to air only led to a 10–15% drop in yield (see SI section 3 for details). While the reported scope was conducted under rigorously dry and air-free conditions, the robustness of this ring contraction to changes in solvent, water, and air makes this protocol straightforward and operationally simple.

Scope of the Reaction.

With optimized conditions in hand, the *N*–aryl scope of the blue-light-mediated ring contraction was explored (Figure 3). Generality with respect to the nature of the photoreactive aroyl group was investigated first. Substrates with aroyl groups bearing electron-donating substituents (affording **17–18**), electron-withdrawing substituents (affording **19–20**), and halide cross-coupling handles (affording **19**) all contracted in consistently high yields over 80% and 20:1 d.r. Steric encumbrance about the aryl ketone, which significantly decreased yield for the sulfonamide substrate class, did not significantly affect the efficiency of the *N*–aryl ring contraction, as evidenced by the formation of **21** in 76% yield and 20:1 d.r. Substrates bearing diverse heteroaryl ketones contracted in high yields and diastereoselectivities (affording **23–25**), as did substrates bearing polycyclic aromatic moieties (affording **22, 26–27**, albeit proceeding with reduced diastereoselectivity for extended heterocyclic aromatic systems).

Nonaromatic ketones also proved to be effective photoreactive handles for ring contraction. Alkenyl ketone **28** was cleanly generated by the ring contraction in 62% yield and 20:1 d.r. Contraction of aliphatic methyl and *n*-butyl ketones, which required shorter wavelength irradiation (med. pressure Hg) due to poorer light absorption in the visible range, afforded desired products **29** and **30** in 44 and 40% yield, respectively, in 20:1 d.r. for both cases. Highlighting the excellent selectivity of this reaction, no undesired side products associated with Norrish I, Norrish II, or Norrish-Yang processes involving the aliphatic *n*-butyl chain were observed alongside **30**, whereas only trace quantities of the Norrish-Yang product involving the α-amino position were observed in the crude mixture.

Next, the scope with respect to substitution on the *N*–Ar group was investigated. Electron-withdrawing substituents (**31–34**), electron-donating substituents (**35–37**), and cross-coupling handles (**33–34**) were all well tolerated, and the products were obtained in very high yields and diastereoselectivity (20:1 d.r.). A moderately bulky *N*–Ar group was well accommodated (**38**, 89% yield, 20:1 d.r.), as was the polycyclic aromatic *N*–naphthyl group (**40**, 54% yield, 20:1 d.r.). Notably, the contraction of an *N*–pyridyl substrate to afford **39** also proceeded in high yield and diastereoselectivity (79%, 20:1 d.r.).

Substrates bearing substituents on the piperidine backbone consistently afforded high yields of the ring-contracted products (**41–43**), albeit as a mixture of epimers at the substituent-bearing stereocenter. The diastereoselectivity in these cases appears to be dictated by the steric bulk of the substituent, as the ratio of epimers correlates with the substituent A-values (—CO_2Me < —Me < —Ph). The energetic penalty for axial placement (leading to the *trans* diastereomer) of the backbone substituent relative to equatorial placement (leading to the *cis* diastereomer) is larger for more sterically demanding substituents, meaning that substituents with larger A-values enforce a stronger conformational bias in the Mannich ring closure that leads to the favored all-*cis* diastereomer.

In addition to the robust ring contraction of piperidine derivatives, other heterocycles, such as morpholine **44**, also successfully contracted under blue-light irradiation to afford **45**. Of note, the enhanced reactivity and selectivity afforded by the *N*–Ar motif enabled the ring contraction of piperazine **48** to pyrrolidine **49**, converting the fourth most common ring system in small-molecule FDA-approved drugs to the eighth most common.[7] Analogous piperazines bearing electron-withdrawing groups on the extruded nitrogen did not previously afford any desired product. *N*–Ar azepane 46 also successfully underwent ring contraction to afford **47**, representing the first expansion of this methodology to include a seven- to six-membered ring contraction–a transformation not possible under the previous substrate manifold. The fused tetrahydroisoquinoline skeleton **50** also undergoes the desired ring contraction in good yield and excellent diastereoselectivity to afford **51**, further demonstrating the breadth of skeletons that can be effectively diversified by using this chemistry.

Finally, a streamlined one-pot process achieves aroylation and ring contraction from the corresponding *N*–Ar piperidine, albeit in reduced yield, for substrates synthesized through photomediated *α*-aroylation (Figure 3B). As a demonstration, one-pot aroylation and ring contraction of *N*– Ph piperidine **52** afforded 37% yield of the desired ring contraction product **16**, along with side products stemming from further reactivity between the extruded amine of the product and excess base or benzoyl chloride (Figure 3B, **53** and **54**, *unoptimized*). For rapid access to novel chemical space, the operational simplicity of this one-pot process may be desirable despite the reduced yields, as it accomplishes the targeted single-atom skeletal edit without necessitating a separate synthetic step to install the photoreactive handle.

Control of Diastereoselectivity.

All substrates tested in the ring contraction afford *cis* products with good to high selectivity under the optimized conditions. This diastereoselectivity is attributed to H-bonding interactions and steric repulsions in the Mannich ring-closing transition state that kinetically favor cis-product formation.[13] We hypothesized that diastereoselectivity could be controlled by changing the reaction conditions to favor the thermodynamic product instead. Indeed, running the ring contraction in polar protic solvents such as MeOH or *i*PrOH, along with the addition of a substoichiometric amount of acid, switches the selectivity of the transformation to favor the *trans*-diastereomer (Figure 4). The addition of acid is required for the switch in selectivity, as simply running the ring contraction in MeOH without the

acid additive results in significant decomposition, lower yields, and 20:1 diastereoselectivity for the *cis* product. The isolated *cis* product can also be converted to the thermodynamically favored *trans* product under similar conditions without the need for irradiation.

There are two mechanistic possibilities for which the trace acid is likely responsible: (1) direct epimerization of the carbonyl α-proton or (2) retro-Mannich ring opening followed by Mannich reclosure that equilibrates to the thermodynamic product. As the conversion of highly enantioenriched *cis* product **16** to the *trans*-diastereomer ***epi*-16** using an achiral acid resulted in the racemic *trans* product (Figure 4, bottom), the epimerization must involve a retro-Mannich/Mannich sequence during which all stereochemical information is ablated. Thus, diastereoselectivity can be conveniently controlled by changing the reaction solvent and adding a trace acid to obtain the thermodynamic product of the ring contraction. The ability to easily access both diastereomers of the ring contraction products enhances the synthetic utility and control over the selectivity of the reaction.

Rationalization of Increased Yields and Diastereoselectivity.

The yields and diastereoselectivities for the contraction of *N*–Ar substrates are significantly enhanced in comparison to those of substrates bearing more strongly electron-withdrawing groups on the piperidine nitrogen (Figure 1B). These contractions essentially all go to completion with a clean reaction profile at generally faster rates and give more photostable products. For example, the installation of an *o*-Me substituent on the photoreactive phenyl ketone leads to dramatically decreased yield and d.r. for the contraction of sulfonamide-type substrates (see **5**, 21% yield, 2:1 d.r.). However, ring contraction of the *N*–Ph variant of the *o*-tolyl ketone afforded **21** with a nearly 4-fold increase in yield and over 20:1 d.r., highlighting the increased robustness of the *N*–Ar contractions to added steric encumbrance on the aroyl group. Nearly all ring contractions of the *N*–Ar class give >20:1 d.r., whereas diastereoselectivities were low to modest for most of the previously investigated substrates bearing electron-withdrawing groups on nitrogen. In line with the observed trend for diastereoselectivity, the average yields for the *N*-aryl substrates are also substantially higher. Even for *N*-aryl substrates bearing alkenyl or aliphatic ketones, which are more challenging substrates that often require higher energy irradiation due to their reduced absorption at 400 nm, the contractions afforded **28–30** in significantly higher yields and diastereoselectivities than their *N*–SO_2Ar counterparts. For example, *N*–Ph methyl ketone **29** was isolated in nearly double the yield relative to the *N*–Ts analogue **8** after a shorter irradiation time.

We hypothesize that a major factor leading to increased yields for the ring contraction of *N*–Ar substrates is their stronger absorbance at 400 nm (Figure 5). The molar extinction coefficient at 400 nm for *N*–Ph substrate **15** is $\varepsilon_{400,\mathrm{N-Ph}} = 0.110 \pm 0.0007\ \mathrm{cm^{-1}mM^{-1}}$, whereas that for the analogous *N*–SO_2Ph substrate **55** is $\varepsilon_{400,\mathrm{N-SO2Ph}} = 0.0016 \pm 0.0004\ \mathrm{cm^{-1}mM^{-1}}$. In addition to enhanced overall absorbance intensity for the $\mathrm{n} \rightarrow \pi^*$ transition, the $\lambda_{\mathrm{max},n\rightarrow\pi^*}$ of **15** is red-shifted by 32 nm relative to the $\lambda_{\mathrm{max},n\rightarrow\pi^*}$ of **55**. The net result is that *N*–Ph substrate **15** absorbs over 67 times more strongly than sulfonamide substrate **55** at 400 nm, where the applied LED irradiation is centered. Much stronger absorbance relative to previously explored substrate classes was also measured for several other *N*–Ar substrates (see SI section 5 for a full discussion of the UV–Vis data). These differences in both the $\lambda_{\mathrm{max},n\rightarrow\pi^*}$

and the magnitude of the molar extinction coefficients are likely due to significant electron donation from the nitrogen lone pair during electronic excitation (*vide infra*).

On the basis of this hypothesis, we postulated that the 3-cyanoumbelliferone additive used in our prior report (see Figures 1-4), which modestly improved yield and diastereoselectivity for a handful of substrates, might do so by enhancing the absorbance of some substrates through the formation of an electron donor–acceptor (EDA) complex.[41,42] Though 3-cyanoumbelliferone is a known triplet sensitizer, the triplet energy is lower than the triplet energies of the substrates, precluding efficient sensitization through Dexter energy transfer.[13,43] UV–Vis analysis of *N*–benzoyl substrate **3** (Figure 1B) both with and without 3-cyanoumbelliferone shows a modestly amplified and red-shifted $n \rightarrow \pi^*$ absorbance band in the presence of 30 mol % of the additive (see SI section 5 for details). Therefore, the subtle substrate-dependent increases in yield noted previously with the 3-cyanoumbelliferone additive are likely due to the formation of EDA complexes with select substrates bearing electron-withdrawing groups on nitrogen that moderately improved the irradiation efficiency for poorly absorbing substrates. This observation is consistent with our hypothesis that stronger absorbance of the *N*–Ar substrates upon irradiation at 400 nm contributes to higher yields.

Another factor that likely leads to enhanced yields and cleaner reaction profiles for the *N*–Ar substrates is the increased photostability of the products. While higher energy irradiation centered at 385 nm caused arylsulfonamide substrates to undergo decomposition and oligomerization due to nonspecific excitation of both the substrate and product,[13] irradiation of *N*–Ph substrate **15** at 385 nm, and even at 375 nm, cleanly led to the desired ring contraction (see below for a discussion of wavelength-dependent reactivity). In fact, irradiating the *N*–Ph product **16** with even higher energy light centered at 365 nm (LED) or broadly ultraviolet light (medium-pressure Hg lamp) for 24 h led to the complete and clean recovery of **16**, further highlighting the photostability of these *N*–Ar ring contraction products. UV–Vis analysis of *N*–Ph product 16 revealed the disappearance of a distinct $n \rightarrow \pi^*$ absorbance feature in the absorption spectrum and significantly lowered molar extinction coefficients relative to substrate **15**.

The significantly higher diastereoselectivity in product formation for the *N*–Ar contractions in comparison to those of substrates bearing electron-withdrawing groups on the azacycle nitrogen is likely due to stronger intramolecular H-bonding between the more basic *N*–Ar imine nitrogen and enol hydrogen in the linear intermediate (see Figure 6).[13] This hydrogen bonding interaction may serve two purposes: first, to preorganize the imine-enol to attain the transition state geometry more easily and, second, to more tightly organize the Mannich ring-closing transition state that leads to the product. These effects would lead to improved diastereoselectivity by amplifying the energetic differences between *cis* and *trans* forming transition states, as well as potentially leading to faster relative rates of the desired Mannich cyclization compared to the rates of undesired decomposition pathways.

Mechanistic Investigation.

The high yields and diastereoselectivities observed for the *N*–Ar substrate class facilitated experimental investigation into mechanistic nuances that had previously proven challenging.

First, the initial rates of reactions were measured for the photomediated ring contraction of model substrate **15** at different concentrations (0.03–0.08 M) to establish the reaction order in substrate (Figure 7A). The measured rates were consistent, indicating that there is no rate dependence on substrate concentration (i.e., the rate is zeroth order with respect to substrate). This observation supports the conclusion that the ring contraction is photon-limited, with the rate of the reaction depending entirely on the efficiency of irradiation–a combination of the efficiency of excitation (absorption of photons) and quantum yield (product molecules formed per absorbed photon). This conclusion is further corroborated by the observed linear dependence of the reaction rate on the power of the light source (Figure 7D), as well as the observation of essentially complete absorption of incident photons based on the molar extinction coefficient at 400 nm determined by UV–Vis analysis (see SI sections 5 and 6 for details).

A kinetic isotope effect (parallel initial rate measurements) was determined by measuring initial rates of reaction for protio substrate **15** and deutero substrate **15-d9** (Figure 7B). The KIE was calculated to be 0.95 ± 0.04, indicating a *slight* 2° inverse effect. Interestingly, this KIE is not consistent with the previously proposed mechanism (Figure 8, bottom), where one would expect a 1° normal KIE from C—H/D bond cleavage during productive relaxation of the excited-state substrates through 1,5-HAT.[44,45] UV–Vis analysis of **15** and **15-d9** demonstrates that deuteration does not alter the absorbance of the substrate; therefore, differences in rate should be indicative of differences in quantum yield. Because the rate of 1,5-HAT (a productive excited-state process) would directly affect quantum yield, which is the rate of productive processes divided by the rates of all possible productive and nonproductive processes from the excited state, a 1° KIE due to C—H/D bond cleavage would be reflected in the overall rate.[43] It is important to note that there are likely multiple other effects of deuteration, for example, on the relative rates of intersystem crossing or nonproductive vibrational relaxation. Therefore, the measured KIE cannot be conclusively attributed solely to effects on productive relaxation rates.[46] For example, deuteration is known to slow the relative rates of vibrational relaxation due to lowered bond vibrational frequencies.[43] The effects of deuteration on the rates of nonproductive processes may explain the slight inverse 2° KIE observed; for example, if vibrational relaxation was suppressed due to deuteration, one could expect **15-d9** to react more efficiently than **15**. However, the effects of deuteration on nonproductive processes that do not involve C—H/D bond cleavage are expected to be 2° and accordingly small in magnitude.[43] As such, measured KIEs for other excited-state HAT processes are more significant (k_H/k_D ~ 3–6, 1° KIE),[44,45] so quenching of the excited state in this reaction likely does not involve C—H/D bond cleavage. Moreover, the observed KIE and zeroth rate order in substrate concentration are inconsistent with the fragmentation of the 1,4-biradical (**IV**) to the imine-enol (**V**) and Mannich ring closure as potential rate-determining steps (Figure 8).

In light of the observed KIE, we propose an alternative electron-transfer/proton-transfer (ET/PT) mechanism involving photoreduction of the ketone by the internal amine in the excited state, followed by deprotonation at the α-position (Figure 8). In this mechanistic proposal, excitation and productive relaxation through electron transfer to generate charge-separated intermediate **III** occur without a concerted C—H/D cleavage event. Deprotonation then affords the same 1,4-biradical **IV** as that proposed in the HAT pathway. Prior investigations by Padwa and co-workers on the photochemistry of related α-aminoacetophenone systems are consistent with this mechanistic conclusion and corroborate the likelihood of the ET/PT pathway predominating over relaxation through HAT.[45,47] It has previously been proposed for related systems that both $n \rightarrow \pi^*$ and $\pi \rightarrow \pi^*$ triplet states can undergo this electron-transfer process.[45] Other mechanistic hypotheses, including C—N bond fragmentation prior to HAT or ET/PT to generate **IV**, were discounted as (1) carbonyls predominantly undergo Norrish I and II processes, (2) the generation of highly reactive aminyl and alkoxy radicals and cleavage of a strong C—N bond without a significant driving force are unfavorable, and (3) premature fragmentation of the ring severs the favorable 1,5 relationship between the α–*N* position and the carbonyl oxygen that would facilitate downstream HAT or proton transfer.[43]

The alternative ET/PT mechanistic proposal is also supported by the lack of observable triplet quenching. The addition of 1,3-cyclohexadiene, a known triplet quencher (E_t = 54 kcal/mol),[47] failed to quench the rate of ring contraction of model substrate **15** (Figure 7C). Moreover, the ring contraction is relatively robust to atmospheric oxygen, which is also a highly efficient triplet quencher for ketones with $\pi \rightarrow \pi^*$ or $n \rightarrow \pi^*$ triplet states.[48] This lack of triplet quenching is consistent with prior observations for related systems and implies that the excited-state reaction and/or relaxation of these substrates is faster than the rate of diffusion (i.e., the excited triplet state reacts or relaxes before encountering a quencher molecule).[45] Though a very rapid HAT pathway cannot be fully discounted, the lack of triplet quenching does not support the existence of long-lived triplet biradicals.

To more completely characterize the photomediated ring contraction, we next turned our attention to measuring the quantum yield. The quantum yield of the ring contraction of *N*–Ph substrate **15** was measured by calibration against the photodecomposition of potassium ferrioxalate, a commonly used chemical actinometer with characterized quantum yields at multiple wavelengths.[49] Following the original procedures from Hatchard and Parker,[49,50] the incident photon flux on a 20 mL scintillation vial (3.6 mL solvent volume) in the Penn PhD m2 photoreactors (400 nm LED insert) was measured to be (2.773×10^{-6}) ± (3.481×10^{-7}) einstein/s. Notably, the measurement of incident photon flux is specific to the reaction setup and is therefore one of the most accurate representations of the irradiation energy used to drive a photochemical reaction.[51,52] On the basis of UV–Vis analysis, >99% of incident light is absorbed by the *N*–aryl substrates at the standard 50 mM reaction concentration; therefore, it is assumed that incident photon flux is completely absorbed by the substrate at low conversions.[42] On the basis of the measured photon flux and initial rate data, the quantum yield of the ring contraction for *N*–Ph substrate **15** was found to be $\Phi = 0.022 \pm 0.002$.

The measured quantum yield is significantly less than one, indicating that there are likely no radical chain processes occurring.[53] Though not conclusive, low quantum yields (e.g., less than 0.15) have also been cited as evidence to support ET/PT mechanisms over HAT due to the high likelihood of facile, unproductive back-electron transfer that returns the charge-separated excited-state substrate (Figure 8, **III**) back to the ground state (Figure 8, **I**).[45] For the photomediated ring contraction, the measured quantum yields are likely even lower than those measured by Padwa et al. for related acyclic systems (approximately 0.05–0.15)[45] because the α-amino ketone motif is partially embedded in a ring system that restricts the possible low-energy conformations. In the lowest energy conformation of the substrates, the aroyl group is oriented pseudoaxially to minimize steric clash with the substituents on nitrogen.[13] This conformation also leads to enhanced orbital overlap between the carbonyl π-system and nitrogen lone pair, likely facilitating facile back-electron transfer that lowers the quantum yield (*vide infra*).

Initial rates and quantum yields for four other substrates (**57–60**) were measured using a microreactor equipped with a 405 nm laser (100 mW) and a power meter that recorded blank power before each reaction and transmitted power during each reaction (Table 1, see SI section 8 for full details). The measurement of initial rates was performed by independently irradiating several reactions for time increments between 0 and 90 s (triplicate runs), then quantifying conversion by HPLC analysis against biphenyl internal standard that does not absorb >300 nm or otherwise interfere with the reaction. The light absorbed by the reaction was calculated as the difference between transmitted power during the reaction and blank power measured before each reaction. The measurement of absorbed light was then used with the rate data to calculate quantum yield. The assumption that essentially all absorbed light is absorbed by the substrate is valid only at low conversions when the substrate is the only species in the reaction that absorbs at 405 nm. This experimental setup enabled streamlined and efficient measurements of rate and quantum yield across several substrates, and the measurement of the quantum yield of the contraction of **15** afforded the same value, within error, as the independent measurement against the ferrioxalate actinometer.

The data reported in Table 1 clearly show that the initial rates are affected directly by both the quantum yield and molar extinction coefficient, with the balance between the two factors ultimately determining the overall rate of reaction (for a given light source). For example, the rate of ring contraction of **57** to afford **18** is less than half that of the model substrate **15**. This difference can be rationalized by the lower quantum yield in combination with a molar extinction coefficient that is approximately half that of **15**. It is challenging to draw rigorous mechanistic conclusions from the measured rate data since the varied substitution patterns likely simultaneously affect several variables, including triplet lifetimes, intersystem crossing rates (e.g., heavy atom effect), and nonproductive relaxation pathways.[45] However, there are a few notable trends that appear to corroborate the revised mechanism.

The increased electron-donating ability of the *para*-substituents on the *N*–aryl motif (—Me > —H > —Cl) correlates with larger molar extinction coefficients at 405 nm and decreased quantum yield. As donation from the nitrogen lone pair contributes significantly to the electronic excitations to the lowest-energy excited states (*vide infra*), we hypothesize that increased electron richness of the nitrogen lone pair enhances the efficiency of this

electronic transition (increasing and red-shifting absorbance) but also accordingly increases the efficiency of the back-electron transfer (decreasing quantum yield). Moreover, the increased electron-donating ability of the *para*-substituents on the aroyl motif (—OMe > —H > —F) correlates with decreased quantum yield. This trend can be rationalized under the current mechanistic paradigm due to the decreased efficiency of carbonyl photoreduction for more electron-rich aryl ketones.

Due to the proposed electron transfer that generates a charge-separated intermediate, one might expect solvent polarity to affect the rates of these reactions. Indeed, the effects of solvent polarity on the relative energy levels of $n \rightarrow \pi^* w$ and $\pi \rightarrow \pi^*$ triplet states of aryl alkyl ketones,[43] the reversibility of HAT,[54] and the quantum yields of α-alkoxyacetophenone Norrish II processes have been well-studied.[55] However, the quantum yields for the contraction of *N*–Ph substrate **15** measured in both THF and PhH were found to be the same. This finding, though unexpected, is consistent with observations by Padwa et al., who studied solvent polarity effects on α-aminoacetophenones.[45]

Ultimately, the experimental data, including the observation of a 2° inverse KIE, lack of triplet quenching, and low quantum yields, all support an electron-transfer/proton-transfer mechanism where the excited-state ketone is photoreduced by the internal amine to form a charge-transfer species at a rate exceeding diffusion control. Though a rapid HAT pathway cannot be fully discounted, the revised ET/PT mechanistic proposal also enables the rationalization of observed reactivity trends with respect to the effects of electronically differentiated substituents on quantum yield and absorbance.

Computational Characterization of Lowest-Energy Excited States.

To gain further insight into these excited-state processes, we conducted density functional theory (DFT) and time-dependent DFT (TDDFT, full linear response) calculations to characterize the ground state HOMO/LUMO and the lowest-energy excited states of *N*–Ph model substrate **15** (Figure 9, ωB97X-D/def2-SVP/THF (PCM) for geometry optimizations, ωB97X-D3(BJ)/def2-TZVP(-F)/THF (PCM) for single-point calculations).

The lowest energy conformer of **15** in the ground state (S0) has the aroyl substituent in a pseudoaxial orientation to minimize steric clash with the substituent on nitrogen, which is consistent with the lowest energy conformations of previously investigated substrates with other *N*-substituents.[13] The HOMO and LUMO are relatively localized, with the HOMO dominated by the *N*-aryl portion of the molecule (nitrogen lone pair, donation into Ph) and the LUMO residing on the aroyl motif (π^* of the conjugated system). Consequently, TDDFT calculation of the lowest energy singlet vertical excitation at the ground state geometry corresponds to an $n \rightarrow \pi^*$ electronic promotion where the electron density is promoted predominantly from the nitrogen and carbonyl oxygen lone pairs to the carbonyl π^* system. In comparison to the expected $n \rightarrow \pi^*$ excitation for isolated carbonyls, which is often thought to occur from the carbonyl lone pairs,[13,43] for these substrates, the nitrogen lone pair contributes significantly to the electronic promotion. Investigation of several other low-energy conformers also afforded similar vertical $n \rightarrow \pi^*$ transitions to S1 that involve the nitrogen lone pair. The calculated energy of the S1 vertical excitation matches the

experimental irradiation wavelength more accurately than that of excitation to any higher excited state (S2, S3, etc.).

The conformationally relaxed excited states were then calculated by TDDFT geometry optimizations, and the optimized geometries of the S1 and T1 states for **15**, along with the corresponding natural transition orbitals (NTOs), are shown in Figure 9. NTOs describe the character of a given excited state by condensing the contributing orbital transitions into a minimal number of hole (i.e., where an electron is promoted from) and particle (i.e., where an electron is promoted to) pairs that constitute the electronic transition.[56,57] Only one significant NTO pair was found per S1 and T1 state. NTO analysis for the S1 state is consistent with the vertical $n \rightarrow \pi^*$ Franck–Condon excitation, where the electron density of the nitrogen lone pair is significantly involved in the electronic promotion to the aroyl π^* system. Intersystem crossing to T2 ($\pi \rightarrow \pi^*$) is typically highly efficient for aryl ketones due to spin–orbit coupling (El Sayed's rules), which then likely relaxes quickly to T1 (Kasha's rule).[43] T1 for **15** is also an $n \rightarrow \pi^*$ state with NTOs similar to S1. Interestingly, since excitation from the HOMO to LUMO is a significant contributor to both the S1 and T1 NTOs, both S1 and T1 states have moderate charge-transfer character, with electron density promoted from the nitrogen lone pair to the aroyl π^*.

The characterization of the Franck–Condon excitation and the S1 and T1 excited states is highly consistent with our empirical observations. The $n \rightarrow \pi^*$ absorbance feature is red-shifted and increased in intensity for substrates with more electron-donating groups on nitrogen (Figure 5 and Table 1) because the nitrogen lone pair is raised in energy, enabling more efficient excitation through electron promotion from the lone pair. Due to the pseudoaxial orientation of the aroyl moiety in the lowest energy conformer, the carbonyl π^* and nitrogen lone pair orbitals are held in close proximity (comparing hole and particle overlap). This conformationally enforced orbital overlap likely leads to more rapid unproductive relaxation through back-electron transfer than acyclic systems, which was observed through the low measured quantum yields (Table 1).[45]

Structural variation of S1 and T1 relative to the ground state also corroborates the revised ET/PT mechanism, as both S1 and T1 states have charge-transfer character akin to that of proposed intermediate **III** (Figure 8). The electron promotion from the nitrogen lone pair favors deprotonation by weakening the α-C—H bond through hyperconjugation. This hyper-conjugative weakening of the α-C—H bond is also discernible in the NTO holes (Figure 9) for both S1 and T1. Moreover, as the molecule progresses from S0 to S1 and T1, the charge-transfer character increases, as demonstrated by calculated electrostatic potential (ESP)-based atomic charges.[58,59] From S0 to T1, the atomic charge on the carbonyl oxygen becomes more negative (−0.04), the charge on nitrogen becomes more positive (+0.13), and the α-hydrogen also becomes more positive (+0.03).

To investigate whether the revised ET/PT mechanism is unique to the *N*–aryl system, TDDFT and NTO analyses were also performed for the *N*–SO_2Ph substrate **55**. The computational results show the same qualitative trends as *N*–Ph substrate **15**, but with less prominent charge-transfer character in the excited states as expected due to reduced electron

density on nitrogen (see SI section 12 for details). The initial vertical $n \rightarrow \pi^*$ excitation to S1 has qualitatively less charge-transfer character, and the optimized S1 NTO hole also has less character drawn from the nitrogen lone pair. Due to the lowered energy of the nitrogen lone pair, the T1 state exhibits more $\pi \rightarrow \pi^*$ character, and the change in atomic charges of the carbonyl oxygen and nitrogen is smaller in magnitude than for **15**. Ultimately, we hypothesize that there is likely a spectrum between ET/PT and HAT mechanisms that may be operative for the photomediated ring contraction. The mechanism for specific substrate classes is presumably dependent on the electron density of the nitrogen, as increasing electron density favors the ET/PT pathway, as well as other potential changes to the excited-state potential energy landscapes caused by different substituents.

Wavelength-Dependent Reactivity.

On the basis of our revised mechanistic proposal, insight into quantum yields, and computational characterization of the lowest-energy excited states, we proceeded to investigate the wavelength-dependent reactivity of this system in more detail. While LED irradiation centered at 400 nm was empirically determined to afford optimal yields for the ring contraction,[13] the substrates do not absorb strongly at 400 nm, with UV–Vis analysis revealing that λ_{max} for the spatially forbidden $n \rightarrow \pi^*$ absorbance is typically at higher energy wavelengths (330–370 nm, Figure 5, see SI section 5 for details). Because LEDs are not highly monochromatic light sources (for example, compared to lasers),[39,60,61] the Penn PhD m2 photoreactor used to run the ring contractions with a 400 nm LED insert emits across a relatively broad range of wavelengths (see SI section 7 for measurement of an emission spectrum). As such, one rationalization for the use of 400 nm LED irradiation, despite the relatively poor substrate absorbance, could be that the ring contraction is simply promoted by a small percentage of higher energy photons from the short-wavelength tail of the emission spectrum. Prior investigation of shorter wavelength LEDs with emission spectra that overlap more significantly with substrate absorbance resulted in poor yields and decomposition, potentially due to unintended decomposition of the *N*–SO_2(aryl) products upon higher-energy excitation.[13]

Alternatively, we hypothesize that the desired reactivity may be intrinsically more efficient at 400 nm compared to wavelengths that are more strongly absorbed. To distinguish between these hypotheses, the initial rates of the ring contraction of model substrate **15** were measured upon irradiation at different wavelengths from 375–415 nm using LEDs with shifted central wavelengths. Initial rate measurements are more representative of intrinsic reaction efficiency than yields, which can be affected by decomposition, premature measurement, or inconsistent losses during workup and purification.[51] The ring contraction of **15** proceeds cleanly with high yields and no observable side reactivity or decomposition of the product, even at shorter wavelengths. In the case of the first hypothesis, one would expect the initial rate of reaction to be the fastest at shorter wavelengths that overlap more significantly with substrate absorbance. In comparison, the observation of faster rates at longer wavelengths would support the second hypothesis, wherein overlap with substrate absorbance does not dictate reaction efficiency.

To truly isolate the effects of different wavelengths, we initially attempted to use a tunable femtosecond pulsed laser to achieve highly monochromatic irradiation (full-width half-maximum of 3.2–3.4 nm) at different wavelengths.[61] However, when we irradiated the reactions with a high enough time averaged power to drive appreciable conversion on a reasonable time scale, we also observed significant decomposition and poor mass recovery likely caused by the extremely high intensities intrinsic to ultrafast lasers. Instead, fiber-coupled LEDs with narrow emission spectra (FWHM of 9–14 nm, approximately 30 mW) were used as a practical alternative that could provide continuous low-field emission. These fiber-coupled LEDs with heat sinks mounted on a temperature-controlled platform were equipped with optical fibers that directed the light through the attached cuvette holders on a stir plate set at 300 rpm. Reactions were run in optical grade cuvettes with a magnetic stir bar such that light emitted through the optical cable passed directly through the cuvette (see SI section 7 for full details). The rate of ring contraction of **15** was measured at 375, 385, 395, 405, and 415 nm. After normalizing the experimentally measured rates by the photon delivery rate of each light source, the normalized rates were plotted against wavelength to prepare a photochemical action plot (Figure 10).[61]

The rate of reaction varies significantly as a function of the irradiation wavelength: LED irradiation centered at 395 and 405 nm afforded the fastest normalized rates, while irradiation at both longer and shorter wavelengths led to lower rates. Upon overlaying the wavelength-dependent rate data with the measured UV–Vis molar extinction spectrum of **15** in the reaction solvent (THF), it is clear that (1) the most efficient reaction occurs with irradiation centered at 395–405 nm, and (2) the photochemical action plot is red-shifted by almost 40 nm in comparison to the molar extinction spectrum. This strong red shift is consistent with observations from photochemical action plots of other reactions investigated by Barner-Kowollik and co-workers[61-64] and ultimately demonstrates that the *UV–Vis absorbance spectrum fails to accurately predict optimum photochemical reactivity for the ring contraction*. Barner-Kowollik et al. note that a similar red shift of the photochemical action plot relative to absorbance has been observed in nearly all systems where wavelength-dependent reactivity has been characterized.[61] For the photomediated ring contraction, although maximum absorbance of the $n \rightarrow \pi^*$ transition for **15** occurs at 366 nm, much longer wavelength irradiation at 395–405 nm actually afforded the fastest rates of reaction.

While the measurement of wavelength-dependent reactivity and construction of photochemical action plots is more common in other fields, such as materials science (e.g., polymer degradation) and solar power development (e.g., photovoltaics), this practice is less common in photochemical organic methods development.[61,65,66] In fact, the consistently observed red shift of photochemical reactivity relative to absorbance directly contradicts common advice to irradiate substrates at the wavelength of maximum absorbance to achieve the best reactivity since molecules should absorb strongly to react most efficiently. Although the pronounced red shift of the photochemical action plot relative to UV–Vis absorbance is a frequently observed phenomenon, it remains unclear as to why this effect occurs.[61] Though our experimental setup enabled a practical evaluation of wavelength-dependent reactivity without access to high-powered lasers, the LED light is not strictly monochromatic. Thus, some of the observed reactivity at longer wavelengths may still be attributable to a minute

fraction of higher energy photons in the emission spectrum. However, this effect does not explain the reduction in rate at shorter wavelengths that are more strongly absorbed, particularly since there was no side reactivity or decomposition observed over the course of these reactions for any wavelength.

There are two potential optical contributions to this red shift. It is possible that scattering effects contribute more to the UV–Vis molar extinction spectra at shorter wavelengths, causing an overestimation of absorption at short wavelengths that leads to the observed red shift.[61] However, scattering cross sections for small molecules are on the order of 10^{-25} cm^2 $molecule^{-1}$, so deviations between absorption and extinction are expected to be minimal.[61] A more significant factor may be differences in the optical penetration depths of short and long wavelengths. Indeed, these reactions are run at high enough concentrations that essentially all incident light is absorbed; therefore, differences in light penetration and the effective irradiated volume are likely non-negligible. However, as the reactions were homogeneous and unimolecular, exhibited low quantum yields, and were agitated during irradiation, significant effects on rate due to differences in optical penetration depth are not expected. Moreover, similar red shifts have been observed even in low-concentration systems where light attenuation through the sample volume was minimal; thus, differences in penetration depth do not fully account for observed discrepancies between absorbance and reaction efficiency.[61]

An “inner filter effect” may be partially responsible for the red shift, wherein over time, the generated product parasitically absorbs and “filters out” light from reaching the remaining substrate. This effect is clearly demonstrated by the quantum yield measurements in Table 1, as the quantum yields measured at high conversion (see for **15** and **60**) are lower than those determined at low conversion. The calculation of quantum yield in this experiment was dependent on the assumption that all absorbed light is absorbed by the substrate. However, this assumption becomes invalid at high conversions. Substrate absorbance is overestimated due to parasitic absorbance by the product, which leads to artificially lowered quantum yield values. This conversion-dependent difference is particularly prominent for *N*–(*p*-chlorophenyl) substrate **60**, where the measured quantum yield at high conversion (through 45%) is just half that measured at low conversion (through 14%). The significant “inner filter effect” observed is consistent with the measured molar extinction spectra of **60** and product **33**. Product **33** absorbs much more strongly at 405 nm than substrate **60** ($\varepsilon_{405\,nm} = 0.1853 \pm 0.0010$ and 0.0846 ± 0.0005 $mM^{-1}cm^{-1}$, respectively), so even the generation of small quantities of product over the course of the reaction significantly decreases the fraction of light absorbed by the substrate.

The “inner filter effect” could contribute to the red shift since the relative absorbance of the products compared to the substrates increases at shorter wavelengths, causing an exacerbated filter effect at shorter wavelengths. For model substrate **15**, the relative absorbance of the substrate compared to the product is maximized at approximately 400 nm and decreases at both shorter and longer wavelengths (Figure 11). In fact, below 375 nm, the product absorbs more strongly (larger molar extinction coefficient) than the substrate.

However, this effect should not significantly affect initial rate measurements through low conversion due to low product concentration, and no significant nonlinearity in rate was observed at <20% conversion. Thus, this effect alone cannot fully account for the observed red shift. From a practical standpoint, the “inner filter effect” does result in diminishing returns with extended irradiation–as the reactions near completion, increasing amounts of light may be required to drive the reaction further. With substrate and product molar extinction coefficients, it is possible to model the progress of the reaction by accounting for decreased productive absorbance over time due to both decreased substrate and increased product concentration (see SI section 10 for details). As the difference between substrate **15** and product **16** absorbance is maximized around 400 nm, this effect may explain, in part, why empirical optimization based on the yield after 24 h afforded 400 nm as the optimal wavelength for this transformation.

In addition to the discussed effects, we postulate that the observed red shift for the photomediated ring contractions may be primarily attributed to excited-state processes. While the productive excitation of excimers or transannular bands formed by π-orbital overlap has been invoked to explain this red shift in other systems,[62,63,67] excimer excitation is likely not a primary factor in our system due to the low concentration and lack of dependence of rate on substrate concentration. In contrast, it is known that the location and dynamics of molecules on excited-state potential energy surfaces, especially near conical intersections, can dramatically influence relaxation outcomes.[68,69] An ensemble of low-energy conformers exists in solution at room temperature, and excitation of different conformers likely requires slightly different irradiation wavelengths and results in the initial excitation to different locations on excited-state potential energy surfaces. We hypothesize that this red shift is due to complex yet subtle changes in the geometry and energy of the excited states that ultimately affect the trajectories and rates of productive and unproductive relaxation.[69] For example, excitation to a point on the excited-state potential energy surface close to productive conical intersections could significantly enhance relative rates of internal conversion to the ground state or intersystem crossing to the triplet state.[43] Alternatively, the strongest absorbance could access an excited state that primarily relaxes through a nonproductive pathway. Especially since there is an ensemble of low-energy conformations in solution at room temperature, excitation of some conformers could populate more productive excited states than others (e.g., a more significant charge-transfer character that accelerates productive relaxation through ET/PT). Though the specific causes of the observed red shift are yet to be completely elucidated, we envision that both the characterization of the red-shift effect in the photomediated ring contraction system and the proposed explanations will serve as a foundation for future investigation and development of related photochemical reactions.

CONCLUSIONS

Our expansion of the photomediated ring contractions to *N*–aryl substrate classes significantly expands the reactivity of this skeletal edit to include electronically differentiated nitrogen heterocycles and previously unsuccessful substrate classes (piperazine, azepane). Significantly higher yields, faster rates, and higher *cis*-diastereoselectivity, even with trace water and air, were achieved by leveraging increased

electron density on nitrogen to enhance n → π^* excitation and strengthen intramolecular H-bonding. Related UV–Vis investigation revealed that the additive 3-cyanoumbelliferone likely acts through the formation of a weak EDA complex that modestly enhances light absorption for select substrates. By applying emerging strategies for the α-aroylation of *N*-aryl heterocycles, we are able to install the photoreactive aroyl handle onto diverse, unfunctionalized *N*-aryl heterocycles, often circumventing the need for substrate synthesis from pre-aroylated precursors. This aroylation also allowed us to demonstrate one-pot aroylation and ring contraction of a model substrate. The diastereoselectivity can be controlled to favor *trans* products by modifying the reaction conditions (polar protic solvents, trace acid) to render the Mannich cyclization reversible.

The improved reactivity profile of the *N*–Ar substrates enabled, for the first time, experimental investigations into the mechanistic intricacies of the photomediated ring contraction. The discussed mechanistic studies are consistent with a revised mechanistic proposal, wherein the requisite 1,4-biradical intermediate is generated through rapid intramolecular photoreduction of the excited-state carbonyl by the nitrogen lone pair followed by deprotonation (ET/PT). The proposed mechanism is additionally corroborated by observed trends in measured quantum yields and molar extinction coefficients for several substrates, as well as computational characterization of modest charge-transfer character in the lowest-energy excited states by TDDFT.

Wavelength-dependent reactivity was characterized by the generation of a photochemical action plot that compares the initial rates of reaction at different wavelengths with the molar extinction spectrum. Notably, the most efficient reactivity was observed at wavelengths almost 40 nm red-shifted from λ_{max} of the n → π^* absorbance feature. Potential contributors to the observed red shift may include differences in optical penetration depth, an “inner filter effect” that was quantitatively demonstrated by differences in measured quantum yield values, and complex potential differences in excited-state processes across an ensemble of low-energy conformers in solution.

We anticipate that this work will not only broadly expand the synthetic utility of the photomediated ring contractions but also provide valuable insights into the fundamental mechanistic and photophysical processes underpinning the observed reactivity. A deeper understanding of the mechanistic nuances and characterization of wavelength-dependent reactivity may enable the rational design and optimization of related photochemical transformations.

Supplementary Material

Refer to Web version on PubMed Central for supplementary material.

ACKNOWLEDGMENTS

The authors thank Dr. Hasan Celik and UC Berkeley’s NMR facility in the College of Chemistry (CoC-NMR) for spectroscopic assistance. Instruments in the CoC-NMR are supported in part by NIH S10OD024998. The authors thank Dr. Nicholas Settineri (UC Berkeley) for X-ray crystallographic studies and are grateful to Dr. Dave Small and Dr. Kathy Durkin from the Molecular Graphics and Computation Facility at UC Berkeley (supported in part by NIH S10OD023532) for computational guidance. The authors thank Zhongrui Zhou from the QB3/Chemistry Mass

Spectrometry Facility at UC Berkeley for high-resolution mass spectrometry and are grateful to Prof. Jonathan Rittle for access to the UV–Vis spectrophotometer, and additionally thank Prof. Bob Bergman for detailed and insightful discussions. The authors acknowledge the help and support of the following people from Merck & Co., Inc., Rahway, NJ, USA: Spencer McMinn, Lisa Nogle, and the Boston purification group for chiral SFC analysis and purification, Pablo Trigo Mouriño and Samantha Burgess for NMR structure elucidation support, and Michael Ryan and Andrew Musacchio for review of the manuscript.

Funding

R.S. is grateful to the National Institute of General Medical Sciences (NIGMS, R35 GM130345) and Merck Sharp & Dohme LLC, a subsidiary of Merck & Co., Inc., Rahway, NJ, USA (MSD). S.F.K. and B.R.N. thank the National Science Foundation for support by the NSF Graduate Research Fellowship Program under Grant No. DGE 1752814. H.S. thanks the Studienstiftung des deutschen Volkes (German Academic Scholarship Foundation) for a scholarship. H.H. thanks the MSD Future Talent program for funding. M.Z. acknowledges funding by the W. M. Keck Foundation, funding from the Hellman Fellows Fund, funding from the UC Office of the President within the Multicampus Research Programs and Initiatives (M21PL3263, M23PR5931), funding from Laboratory Directed Research and Development Program at Berkeley Lab (107573 and 108232), and the National Science Foundation (DMR-2247363).

REFERENCES

(1). Castellino NJ; Montgomery AP; Danon JJ; Kassiou M Late-Stage Functionalization for Improving Drug-like Molecular Properties. Chem. Rev 2023, 123, 8127–8153. [PubMed: 37285604]

(2). Peplow M. Skeleton Crew. Nature 2023, 618, 21–24. [PubMed: 37259000]

(3). Jurczyk J; Woo J; Kim SF; Dherange BD; Sarpong R; Levin MD Single-Atom Logic for Heterocycle Editing. Nat. Synth 2022, 1, 352–364. [PubMed: 35935106]

(4). Campos KR; Coleman PJ; Alvarez JC; Dreher SD; Garbaccio RM; Terrett NK; Tillyer RD; Truppo MD; Parmee ER The Importance of Synthetic Chemistry in the Pharmaceutical Industry. Science 2019, 363, No. eaat0805. [PubMed: 30655413]

(5). Qureshi MH; Williams R; Marshall C; Njardarson JT Top 200 Small Molecule Pharmaceuticals by Retail Sales in 2021. J. Chem. Educ 2010, 87, 1348.

(6). Vitaku E; Smith DT; Njardarson JT Analysis of the Structural Diversity, Substitution Patterns, and Frequency of Nitrogen Heterocycles among U.S. FDA Approved Pharmaceuticals: Mini-perspective. J. Med. Chem 2014, 57, 10257–10274. [PubMed: 25255204]

(7). Shearer J; Castro JL; Lawson ADG; MacCoss M; Taylor RD Rings in Clinical Trials and Drugs: Present and Future. J. Med. Chem 2022, 65, 8699–8712. [PubMed: 35730680]

(8). Lovering F; Bikker J; Humblet C Escape from Flatland: Increasing Saturation as an Approach to Improving Clinical Success. J. Med. Chem 2009, 52, 6752–6756. [PubMed: 19827778]

(9). Bhutani P; Joshi G; Raja N; Bachhav N; Rajanna PK; Bhutani H; Paul AT; Kumar RUS FDA Approved Drugs from 2015–June 2020: A Perspective. J. Med. Chem 2021, 64, 2339–2381. [PubMed: 33617716]

(10). Lombardino JG; Lowe JA The Role of the Medicinal Chemist in Drug Discovery – Then and Now. Nat. Rev. Drug Discovery 2004, 3, 853–862. [PubMed: 15459676]

(11). Böhm H-J; Flohr A; Stahl M Scaffold Hopping. Drug Discovery Today Technol. 2004, 1, 217–224.

(12). Wang B; Perea MA; Sarpong R Transition Metal-Mediated C—C Single Bond Cleavage: Making the Cut in Total Synthesis. Angew. Chem, Int. Ed 2020, 59, 18898–18919.

(13). Jurczyk J; Lux MC; Adpressa D; Kim SF; Lam Y; Yeung CS; Sarpong R Photomediated Ring Contraction of Saturated Heterocycles. Science 2021, 373, 1004–1012. [PubMed: 34385352]

(14). Bartholomew GL; Carpaneto F; Sarpong R Skeletal Editing of Pyrimidines to Pyrazoles by Formal Carbon Deletion. J. Am. Chem. Soc 2022, 144, 22309–22315. [PubMed: 36441940]

(15). Kennedy SH; Dherange BD; Berger KJ; Levin MD Skeletal Editing through Direct Nitrogen Deletion of Secondary Amines. Nature 2021, 593, 223–227. [PubMed: 33981048]

(16). Reisenbauer JC; Green O; Franchino A; Finkelstein P; Morandi B Late-Stage Diversification of Indole Skeletons through Nitrogen Atom Insertion. Science 2022, 377, 1104–1109. [PubMed: 36048958]

(17). Dherange BD; Kelly PQ; Liles JP; Sigman MS; Levin MD Carbon Atom Insertion into Pyrroles and Indoles Promoted by Chlorodiazirines. J. Am. Chem. Soc 2021, 143, 11337–11344. [PubMed: 34286965]

(18). Kelley BT; Walters JC; Wengryniuk SE Access to Diverse Oxygen Heterocycles via Oxidative Rearrangement of Benzylic Tertiary Alcohols. Org. Lett 2016, 18, 1896–1899. [PubMed: 27023314]

(19). Collins JL; Staveness D; Sowden MJ; Stephenson CRJ A One-Pot Photochemical Method for the Generation of Functionalized Aminocyclopentanes. Org. Lett 2022, 24, 4344–4348. [PubMed: 35700154]

(20). Dai Y; Huang H; Liang S; Yin Y; Ban X; Zhao X; Jiang Z Catalytic Asymmetric Intermolecular [3 + 2] Photocycloaddition of Cyclopropylamines with Electron-Deficient Olefins. Org. Lett 2023, 25, 4551–4555. [PubMed: 37306259]

(21). Dutta S; Li B; Rickertsen DRL; Valles DA; Seidel D C—H Bond Functionalization of Amines: A Graphical Overview of Diverse Methods. SynOpen 2021, 05, 173–228.

(22). Fernández DF; González-Esguevillas M; Keess S; Schäfer F; Mohr J; Shavnya A; Knauber T; Blakemore DC; MacMillan DWC Redefining the Synthetic Logic of Medicinal Chemistry. Photoredox-Catalyzed Reactions as a General Tool for Aliphatic Core Functionalization Org. Lett 2023.

(23). Chen W; Cao X; Yang X Transition-Metal-Free Methods for the Remote C—H Bond Functionalization of Cyclic Amines. Asian J. Org. Chem 2023, 12, No. e202200547.

(24). Sodano TM; Combee LA; Stephenson CRJ Recent Advances and Outlook for the Isosteric Replacement of Anilines. ACS Med. Chem. Lett 2020, 11, 1785–1788. [PubMed: 33062152]

(25). Mitchell EA; Peschiulli A; Lefevre N; Meerpoel L; Maes BUW Direct α-Functionalization of Saturated Cyclic Amines. Chem. - Eur. J 2012, 18, 10092–10142. [PubMed: 22829434]

(26). Joe CL; Doyle AG Direct Acylation of C(Sp^3)—H Bonds Enabled by Nickel and Photoredox Catalysis. Angew. Chem., Int. Ed 2016, 55, 4040–4043.

(27). Xu G-Q; Xiao T-F; Feng G-X; Liu C; Zhang B; Xu P-F Metal-Free α-C(Sp^3)–H Aroylation of Amines via a Photoredox Catalytic Radical–Radical Cross-Coupling Process. Org. Lett 2021, 23, 2846–2852. [PubMed: 33764790]

(28). Chen M; Ventura AM; Das S; Ibrahim AF; Zimmerman PM; Montgomery J Oxidative Cross Dehydrogenative Coupling of *N*-Heterocycles with Aldehydes through C(Sp^3)–H Functionalization. J. Am. Chem. Soc 2023, 145, 20176–20181. [PubMed: 37672664]

(29). DiRocco DA; Rovis T Catalytic Asymmetric α-Acylation of Tertiary Amines Mediated by a Dual Catalysis Mode: N-Heterocyclic Carbene and Photoredox Catalysis. J. Am. Chem. Soc 2012, 134, 8094–8097. [PubMed: 22548244]

(30). Kessar SV; Singh P; Singh KN; Singh SK Facile α-Deprotonation–Electrophilic Substitution of Quinuclidine and DABCO. Chem. Commun 1999, 1927–1928.

(31). Whisler MC; MacNeil S; Snieckus V; Beak P Beyond Thermodynamic Acidity: A Perspective on the Complex-Induced Proximity Effect (CIPE) in Deprotonation Reactions. Angew. Chem., Int. Ed 2004, 43, 2206–2225.

(32). Chatani N; Asaumi T; Ikeda T; Yorimitsu S; Ishii Y; Kakiuchi F; Murai S Carbonylation at Sp^3 C—H Bonds Adjacent to a Nitrogen Atom in Alkylamines Catalyzed by Rhodium Complexes. J. Am. Chem. Soc 2000, 122, 12882–12883.

(33). Chatani N; Asaumi T; Yorimitsu S; Ikeda T; Kakiuchi F; Murai S $Ru_3(CO)_{12}$ -Catalyzed Coupling Reaction of Sp^3 C—H Bonds Adjacent to a Nitrogen Atom in Alkylamines with Alkenes. J. Am. Chem. Soc 2001, 123, 10935–10941. [PubMed: 11686697]

(34). Peschiulli A; Smout V; Storr TE; Mitchell EA; Eliáš Z; Herrebout W; Berthelot D; Meerpoel L; Maes BUW Ruthenium-Catalyzed α-(Hetero)Arylation of Saturated Cyclic Amines: Reaction Scope and Mechanism. Chem. - Eur. J 2013, 19, 10378–10387. [PubMed: 23780756]

(35). Ryder ASH; Cunningham WB; Ballantyne G; Mules T; Kinsella AG; Turner-Dore J; Alder CM; Edwards LJ; McKay BSJ; Grayson MN; Cresswell AJ Photocatalytic α-Tertiary Amine Synthesis via C—H Alkylation of Unmasked Primary Amines. Angew. Chem., Int. Ed 2020, 59, 14986–14991.

(36). Zhu JL; Schull CR; Tam AT; Rentería-Gómez Á; Gogoi AR; Gutierrez O; Scheidt KA Photoinduced Acylations Via Azolium-Promoted Intermolecular Hydrogen Atom Transfer. J. Am. Chem. Soc 2023, 145, 1535–1541. [PubMed: 36625715]

(37). Capaldo L; Ravelli D; Fagnoni M Direct Photocatalyzed Hydrogen Atom Transfer (HAT) for Aliphatic C—H Bonds Elaboration. Chem. Rev 2022, 122, 1875–1924. [PubMed: 34355884]

(38). Londregan AT; Jennings S; Wei L Mild Addition of Nucleophiles to Pyridine-*N*-Oxides. Org. Lett 2011, 13, 1840–1843. [PubMed: 21375291]

(39). "Chip" Le C; Wismer MK; Shi Z-C; Zhang R; Conway DV; Li G; Vachal P; Davies IW; MacMillan DWC A General Small-Scale Reactor To Enable Standardization and Acceleration of Photocatalytic Reactions. ACS Cent. Sci 2017, 3, 647–653. [PubMed: 28691077]

(40). Smith MT Advances in Understanding Benzene Health Effects and Susceptibility. Annu. Rev. Public Health 2010, 31, 133–148. [PubMed: 20070208]

(41). Tasnim T; Ayodele MJ; Pitre SP Recent Advances in Employing Catalytic Donors and Acceptors in Electron Donor–Acceptor Complex Photochemistry. J. Org. Chem 2022, 87, 10555–10563. [PubMed: 35904501]

(42). Crisenza GEM; Mazzarella D; Melchiorre P Synthetic Methods Driven by the Photoactivity of Electron Donor–Acceptor Complexes. J. Am. Chem. Soc 2020, 142, 5461–5476. [PubMed: 32134647]

(43). Anslyn EV; Dougherty DA Modern Physical Organic Chemistry; University Science Books, 2006.

(44). Xiong Y; Großkopf J; Jandl C; Bach T Visible Light-Mediated Dearomative Hydrogen Atom Abstraction/Cyclization Cascade of Indoles. Angew. Chem., Int. Ed 2022, 61, No. e202200555.

(45). Padwa A; Eisenhardt W; Gruber R; Pashayan D Electron Transfer in the Type II Photoelimination of α-Aminoacetophenones. J. Am. Chem. Soc 1971, 93, 6998–7005.

(46). Beeby A; Parker AW; Simpson MSC; Phillips D Deuteration Effects on the Photophysical Properties of Molecules. J. Photochem. Photobiol., B 1993, 17, 205–207.

(47). Padwa A; Eisenhardt W; Gruber R; Pashayan D Evidence for Electron Transfer in the Photochemistry of π-π^* Triplet States. J. Am. Chem. Soc 1969, 91, 1857–1859.

(48). Grewer C; Brauer H-D Mechanism of the Triplet-State Quenching by Molecular Oxygen in Solution. J. Phys. Chem. A 1994, 98, 4230–4235.

(49). Hatchard CG; Parker CA A New Sensitive Chemical Actinometer - II. Potassium Ferrioxalate as a Standard Chemical Actinometer. Proc. R. Soc. London, Ser. A 1956, 235, 518–536.

(50). Determine photon flux using actinometry HepatoChem. https://www.hepatochem.com/determine-photon-flux-using-actinome-try/ (accessed 26 Sep, 2023).

(51). Noël T; Zysman-Colman E The Promise and Pitfalls of Photocatalysis for Organic Synthesis. Chem. Catalysis 2022, 2, 468–476.

(52). Comparing Commercial Photoreactors - HepatoChem. https://www.hepatochem.com/comparing-commercial-photoreactors/ (accessed 30 Oct, 2023).

(53). Cismesia MA; Yoon TP Characterizing Chain Processes in Visible Light Photoredox Catalysis. Chem. Sci 2015, 6, 5426–5434. [PubMed: 26668708]

(54). Wagner PJ Solvent Effects on Type II Photoelimination of Phenyl Ketones. J. Am. Chem. Soc 1967, 89, 5898–5901.

(55). Lewis FD; Turro NJ Molecular Photochemistry. XVIII. Type II Photoelimination and 3-Oxetanol Formation from α-Alkoxyacetophenones and Related Compounds. J. Am. Chem. Soc 1970, 92, 311–320.

(56). Martin RL Natural Transition Orbitals. J. Chem. Phys 2003, 118, 4775–4777.

(57). 7.13.2 Natural Transition Orbitals; 7.13 Visualization of Excited States; Chapter 7 Open-Shell and Excited-State Methods; Q-Chem 5.2 User's Manual. https://manual.q-chem.com/5.2/Ch7.S13.SS2.html (accessed 03 Nov, 2023).

(58). Momany FA Determination of Partial Atomic Charges from Ab Initio Molecular Electrostatic Potentials. Application to Formamide, Methanol, and Formic Acid. J. Phys. Chem. A 1978, 82, 592–601.

(59). Cox SR; Williams DE Representation of the molecular electrostatic potential by a net atomic charge model. J. Comput. Chem 1981, 2, 304–323.

(60). Arecchi AV; Messadi T; Koshel RJ Light Emitting Diodes (LEDs). In Field Guide to Illumination; SPIE Press: Bellingham, WA, 2007.

(61). Irshadeen IM; Walden SL; Wegener M; Truong VX; Frisch H; Blinco JP; Barner-Kowollik C Action Plots in Action: In-Depth Insights into Photochemical Reactivity. J. Am. Chem. Soc 2021, 143, 21113–21126. [PubMed: 34859671]

(62). Feist F; Walden SL; Alves J; Kunz SV; Micallef AS; Brock AJ; McMurtrie JC; Weil T; Blinco JP; Barner-Kowollik CWavelength-Gated Photochemical Synthesis of Phenalene Diimides. Angew. Chem., Int. Ed 2021, 60, 10402–10408.

(63). Menzel JP; Noble BB; Lauer A; Coote ML; Blinco JP; Barner-Kowollik C Wavelength Dependence of Light-Induced Cycloadditions. J. Am. Chem. Soc 2017, 139, 15812–15820. [PubMed: 29024596]

(64). Menzel JP; Noble BB; Blinco JP; Barner-Kowollik C Predicting Wavelength-Dependent Photochemical Reactivity and Selectivity. Nat. Commun 2021, 12, No. 1691. [PubMed: 33727558]

(65). Kim SH; Stair PC; Weitz E Substrate-Mediated Photodesorption from Multilayers of CH_3I on TiO_2(110) at 90 K. Chem. Phys. Lett 1999, 302, 511–516.

(66). Kim SH; Stair PC; Weitz E UV-Induced Desorption of CH_3X (X = I and Br)/TiO_2(110). J. Chem. Phys 1998, 108, 5080–5088.

(67). Shizuka H; Ishii Y; Hoshino M; Morita T Wavelength-Dependent Photochemical Behavior in 9,10-Dimethylenebianthracene. J. Phys. Chem. A 1976, 80, 30–32.

(68). Corrales ME; González-Vázquez J; Balerdi G; Solá IR; de Nalda R; Bañares L Control of Ultrafast Molecular Photodissociation by Laser-Field-Induced Potentials. Nat. Chem 2014, 6, 785–790. [PubMed: 25143213]

(69). Feng Z; Guo W; Kong W-Y; Chen D; Wang S; Tantillo DJ Analogies between Photochemical Reactions and Ground-State Post-Transition-State Bifurcations Shed Light on Dynamical Origins of Selectivity. Nat. Chem 2024, 1–9. [PubMed: 38123843]

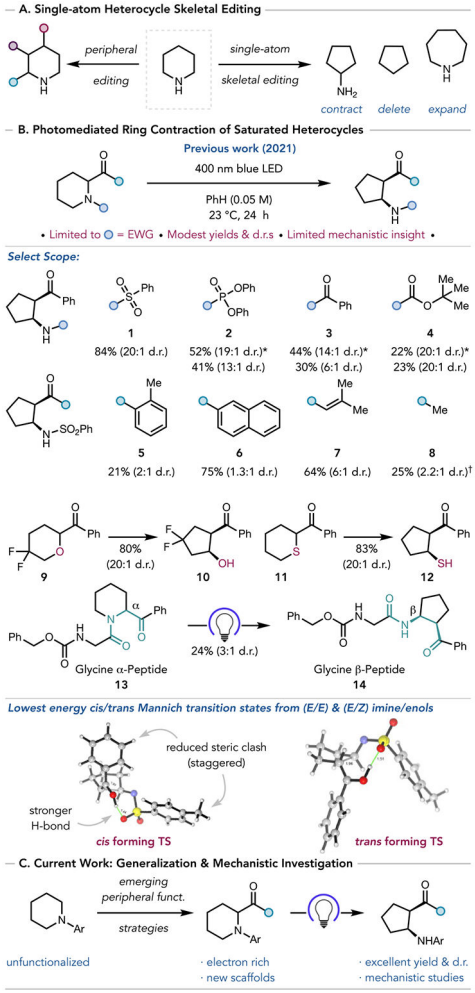

Figure 1.

(a) Single-atom skeletal editing vs peripheral editing. (b) An abbreviated summary of previous work on the photomediated ring contractions of saturated heterocycles. *3-cyanoumbelliferone (30 mol %) added. †Med. pressure Hg lamp for 24 h. (c) Conceptual outline of this work.

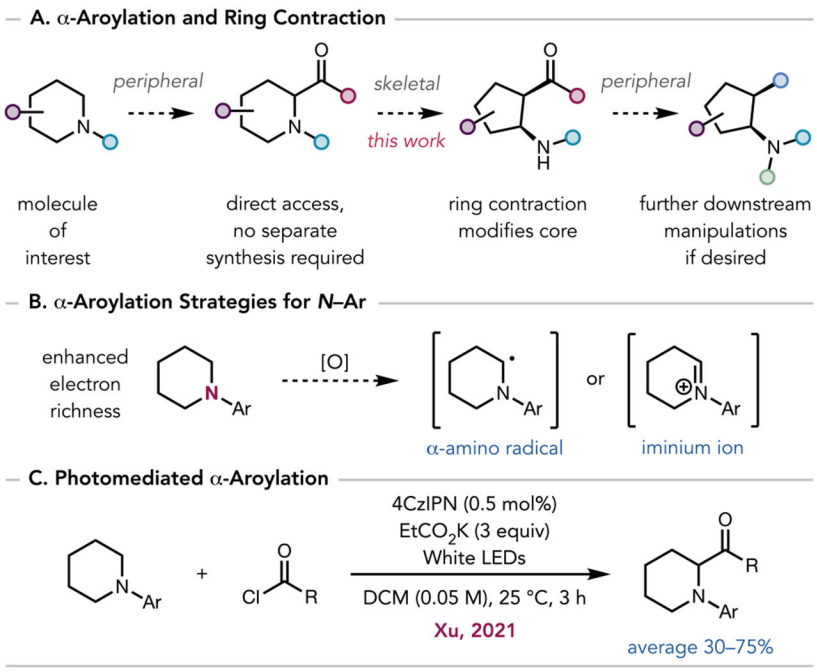

Figure 2.

Synthetic strategies for substrate preparation. (a) Conceptual outline of peripheral to skeletal editing strategy. (b) Conceptual outline of α-functionalization strategies for *N*-aryl piperidines. (c) Photomediated α-aroylation from Xu and co-workers.[27]

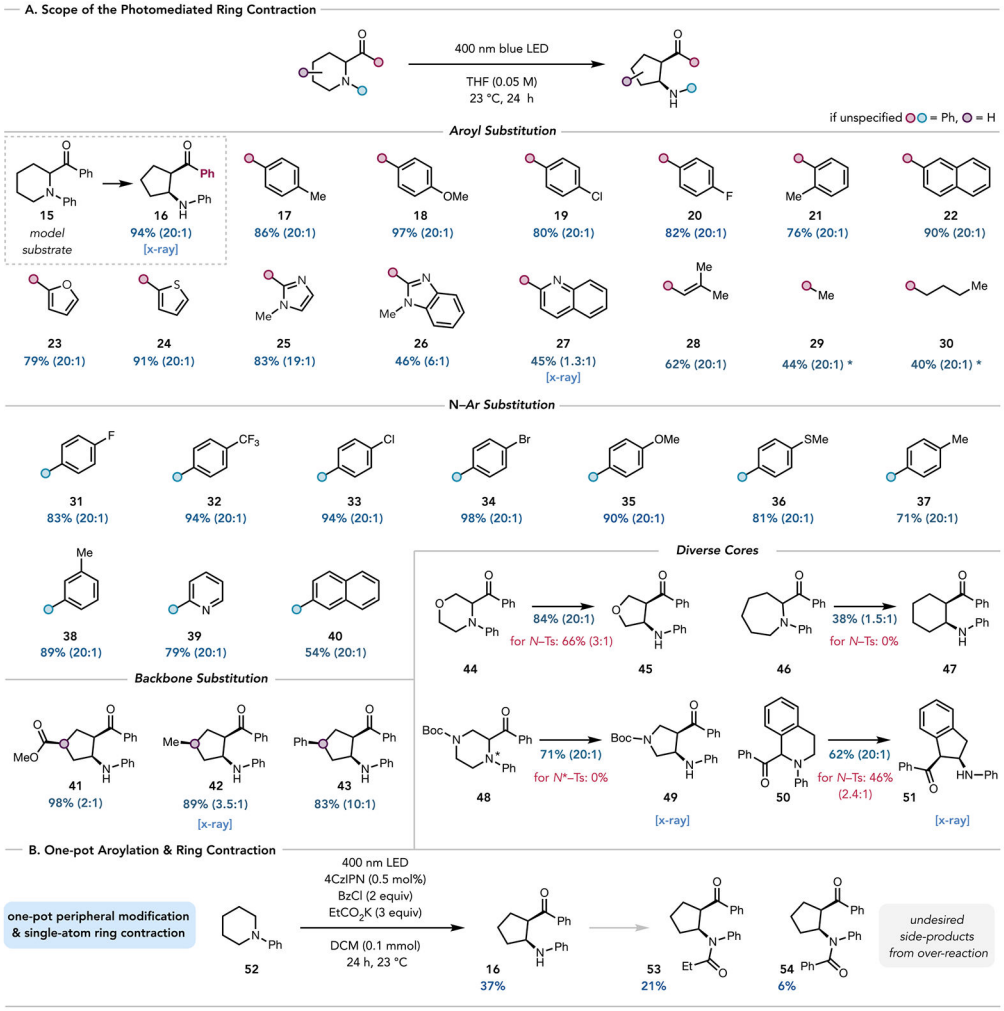

Figure 3.

(a) Ring contraction scope. Reactions were performed on a 0.1 mmol scale. Isolated yields are reported, and relative stereochemistry is shown. Diastereomeric ratios were determined by ^{1}H NMR integration of resonances corresponding to diastereomers in the crude. *Irradiated with a medium-pressure mercury lamp in a quartz tube for 6 (**30**) or 7 (**29**) hours. (b) One-pot aroylation and ring contraction. Reaction performed on a 0.1 mmol scale. NMR yield against Ph_3CH internal standard reported.

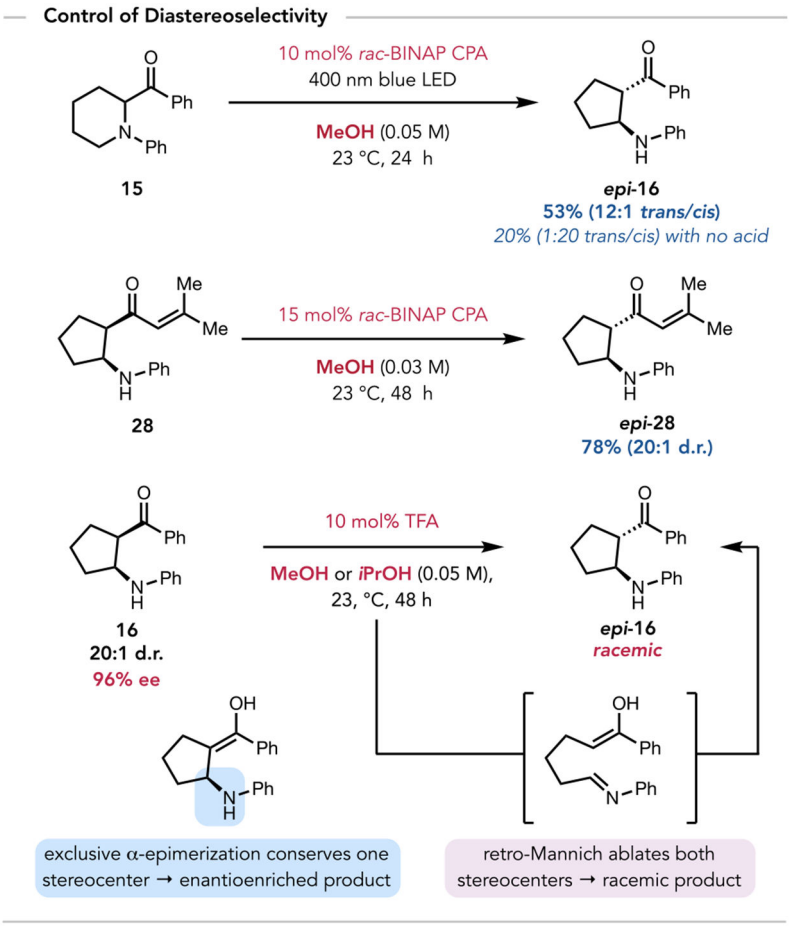

Figure 4.

Demonstration of control over diastereoselectivity by the choice of reaction conditions and associated mechanistic probe.

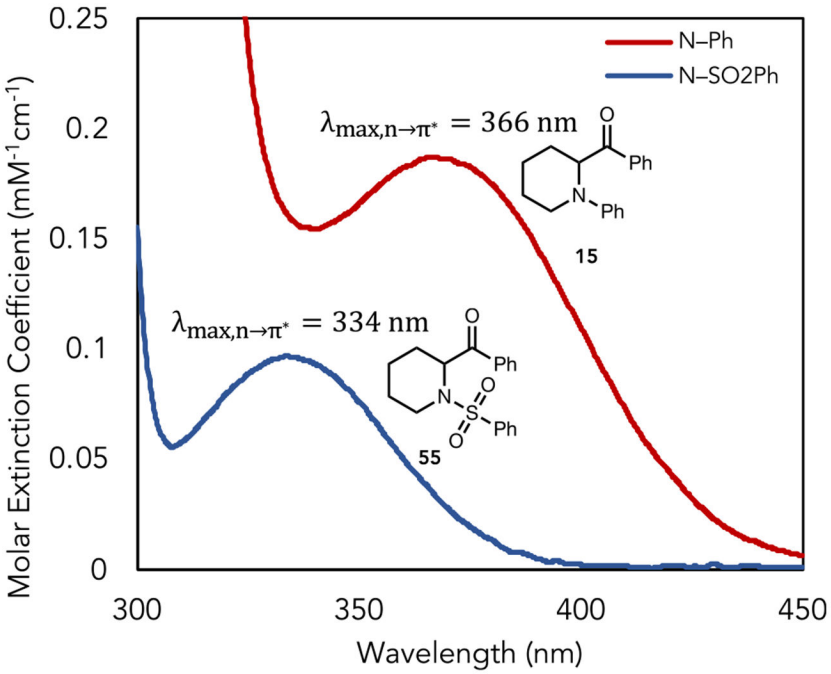

Figure 5.

Molar extinction coefficients for *N*–Ph and *N*–SO_2Ph substrates **15** and **55** from 300–450 nm with λ_{max} values for the $n \rightarrow \pi^*$ absorbance band of interest. ε was calculated from five UV–Vis absorption spectra of different concentrations for each substrate.

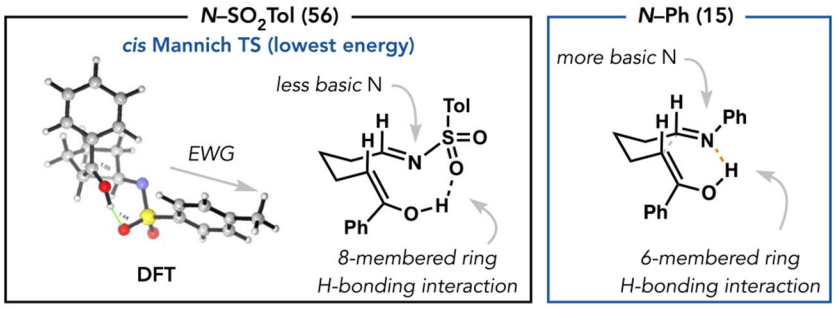

Figure 6.

Comparison of the H-bonding interaction in Mannich ring-closing transition states for *N*–SO_2Tol (**56**) and *N*–Ph (**15**) substrates.

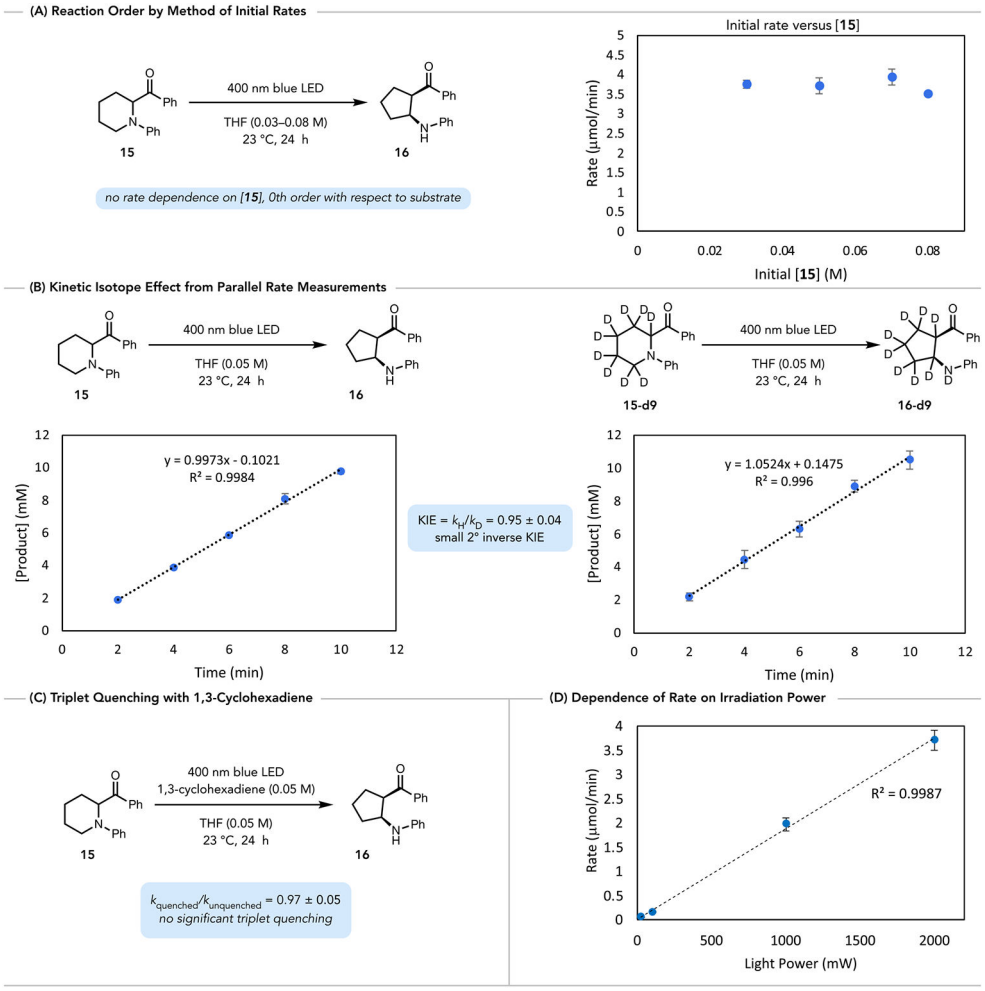

Figure 7.

Mechanistic experiments. (a) The reaction order in substrate was obtained using the method of initial rates and determined to be zeroth order. (b) KIE was obtained by parallel measurement of initial rates for separate reactions. (c) No triplet quenching was observed with 1,3-cyclohexadiene (0.05 M). (d) Linear dependence of the reaction rate on the wattage of the light source for the contraction of **15** at standard 50 mM concentration.

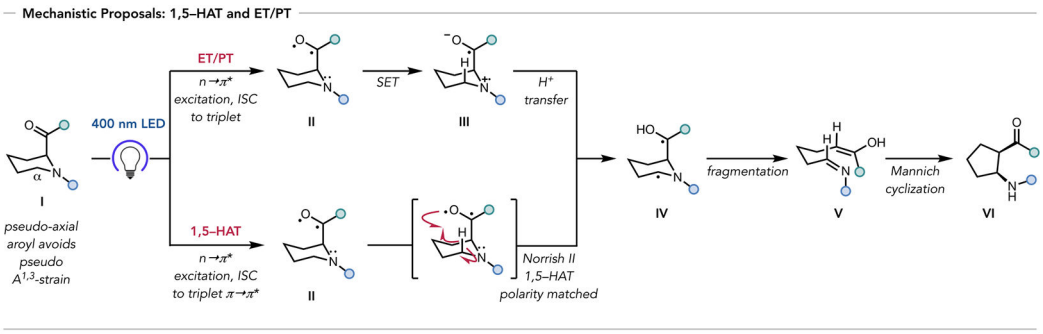

Figure 8.
Proposed mechanism depicting both 1,5-HAT and ET/PT pathways.

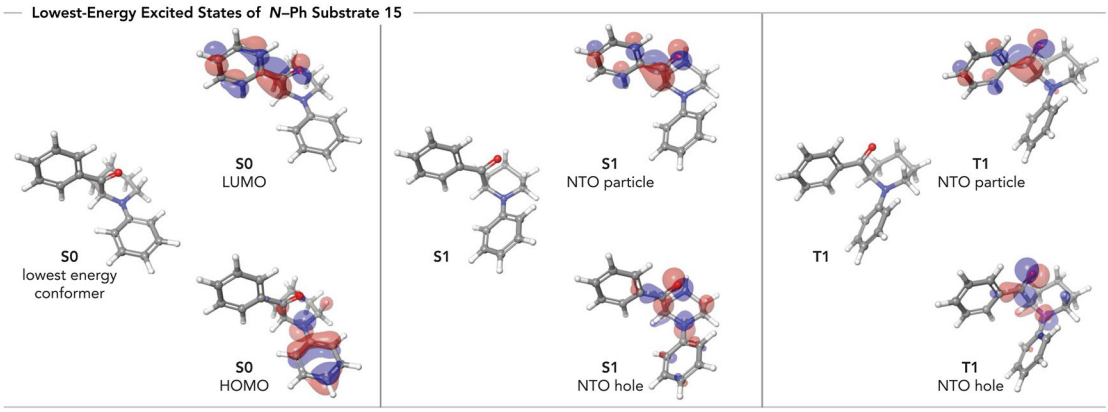

Figure 9.

Optimized structures for S0 (ground electronic state), S1 (lowest singlet excited state), and T1 (lowest triplet excited state) of **15**, with HOMO and LUMO surfaces depicted for S0 and the most significantly contributing NTO hole-particle pairs depicted for the excited states.

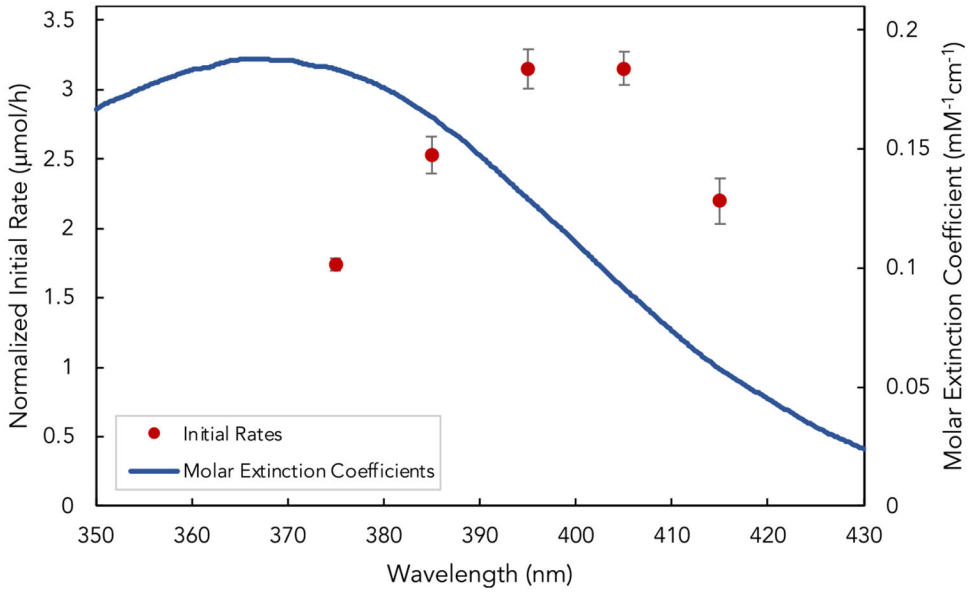

Figure 10.

Characterization of wavelength-dependent reactivity. Initial rates of the photomediated ring contraction as a function of wavelength are plotted over the molar extinction spectrum of **15** in the reaction solvent (THF).

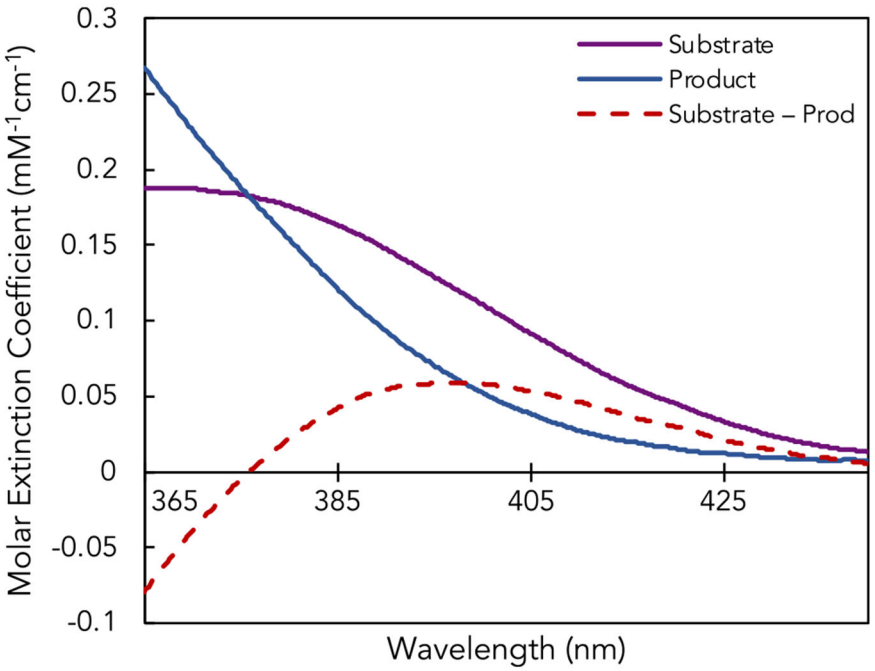

Figure 11.

Molar extinction spectra of *N*–Ph substrate **15**, product **16**, and their difference (substrate minus product) across wavelengths of interest.

Table 1.

Initial Rates, Quantum Yields, and Molar Extinction Coefficients of Substrates at 405 nm[a]

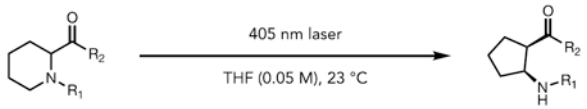

substrate → product	R_1	R_2	initial rate (mmol/h)[b]	quantum yield	ε (405 nm) ($mM^{-1}cm^{-1}$)[g]
15 → 16	Ph	Ph	0.0083 ± 0.0005	0.021 ± 0.002	0.091 ± 0.0007
				0.021 ± 0.004[c]	
				0.022 ± 0.002[d]	
				0.018 ± 0.001[e]	
57 → 18	Ph	(*para*-OMe)Ph	0.0032 ± 0.000i	0.017 ± 0.001	0.045 ± 0.0008
58 → 20	Ph	(*para*-F)Ph	0.0073 ± 0.0002	0.024 ± 0.002	0.082 ± 0.0002
59 → 37	(*para*-Me)Ph	Ph	0.0077 ± 0.0004	0.017 ± 0.001	0.109 ± 0.0006
60 → 33	(*para*-Cl)Ph	Ph	0.0108 ± 0.0006	0.034 ± 0.002	0.085 ± 0.0005
				0.017 ± 0.001[f]	

[a] Initial rates reported as mmol/h, average of triplicate measurements, determined <20% conversion. Quantum yields reported as average of triplicate measurements, determined <20% conversion unless otherwise noted. Conversion monitored by HPLC against biphenyl internal standard.

[b] Reported rates are normalized for 70 mW power.

[c] Measured in PhH (0.05 M).

[d] Measured by calibration against photodecomposition of $K_3Fe(C_2O_4)_3$.

[e] Determined at high conversion (40–60%).

[f] Determined at high conversion (15–45%).

[g] Molar extinction coefficients of substrates at 405 nm were reported as mM^{-1} cm^{-1} in THF.